GSA DATA REPOSITORY 2015066 **McGowan et al.**

Appendix DR1 Analytical Methods

1.1 Major-element EMP preparation and analysis
1.2 Trace-element LAM-ICP-MS preparation and analysis
1.3 Os-Ir-Ru sulphide preparation and analysis
1.4 Zircon preparation and analysis
1.5 $Fe^{3+}/\Sigma Fe$ Mössbauer spectroscopy preparation and analysis

Appendix DR2 Analytical Results for Chromitite

2.1 Major element EMP data for chromite
2.2 Trace element LAM-ICP-MS data for chromite
2.3 $Fe^{3+}/\Sigma Fe$ Mössbauer spectroscopy data for chromite

Appendix DR 3 Ca and Si inclusions

3.1 Light microscope images for Ca and Si inclusions in chromite
3.2 Major element EMP data for Ca and Si inclusions in chromite

Appendix DR 4 Analytical Results for laurites (Os-Ir-Ru sulphides)

4.1 BSE image data for laurites
4.2 Major element EMP data for laurites
4.3 *In situ* Re-Os isotope data for laurites

Appendix DR 5 Analytical Results for Zircons

5.1 BSE and CL image data for zircons
5.2 *In situ* trace element LAM-ICP-MS data for zircons
5.3 U-Pb age LAM-ICP-MS data for zircons
5.4 Hf- and O-isotope LAM-ICP-MS and LAM-MC-ICP-MS data for zircons

Appendix DR 6 Thermo-mechanical Model

Appendix DR 1 Analytical Methods

Unless otherwise stated, all analyses were undertaken at the Geochemical Analysis Unit of CCFS/ GEMOC, Macquarie University, Sydney, Australia.

1.1 Major-element EMP preparation and analysis

Major-element compositions of chromite and silicates were analysed on polished thin sections (30 µm) or polished thick sections (100 µm) using a CAMECA SX100 electron microprobe (EMP) with five wavelength dispersive spectrometers. Analyses used a focused beam (1-2 µm), an accelerating voltage of 15 kV and a beam current of 20-50 nA. Lower limits of detection (LLD) are ≤0.02 wt% oxide for all elements except Fe (0.06 wt%), Ni (0.04 wt%) and Zn (0.08 wt%). Calibration standards used were: albite (Na), Fe_2O_3 (Fe), kyanite (Al), olivine (Mg), chromium metal (Cr), orthoclase (K), wollastonite (Ca, Si), TiO_2 (Ti), Ni metal (Ni), V metal (V), and zinc sulphide (Zn).

Note: Only massive and nodular chromitites were included in the datasets because they are less likely than disseminated chromite to re-equilibrate with matrix olivine during cooling/uplift (González-Jiménez et al., 2013a).

1.2 Trace element LAM-ICP-MS preparation and analysis

Trace-element compositions of chromite and silicate minerals were measured on polished thick sections (100 µm) using a Photon Machines Excite excimer 193 nm laser ablation microprobe system coupled to a 7700 Agilent inductively coupled plasma-mass spectrometer (ICP-MS). Analyses used 40-65 µm beam sizes and intensity of 10.6 J cm^{-2}. The external standards used were NIST 610 and 612 glass (National Institute of Standard and Technology), basalt from Columbia River BCR-2, and Lace Mine chromitites LCR-1 and LCR-2. The Al concentration (measured by EMP) was used as the internal standard for chromitite analyses, and Si concentration (measured by EMP) as the internal standard for silicate analyses. Data were reduced using the GLITTER software (www.mq.edu.au/GEMOC/) for processing time-resolved signals; hardware, operating conditions and methods are otherwise as described by Norman et al. (1996) and Norman et al. (1998).

1.3 Os-Ir-Ru sulphide preparation and analysis

20 grains of the laurite (RuS_2)-erlichmanite (OsS_2) solid solution series platinum group minerals (PGMs) (ranging from 5 to 15 µm) were located in polished thin sections and blocks using reflected light microscopy, and identified using energy dispersive (EDS) x-ray spectra. Back-scattered images were taken for each grain using a variable-pressure scanning electron microscope (VP-SEM) (fig. 4.1.1).

Major-element compositions of PGMs were obtained on polished blocks using a CAMECA SX100 electron microprobe (EMP) following the method described in section 1.1. *In situ* Re–Os isotopic analyses were measured on a New Wave/Merchantek UP 213 laser ablation microprobe coupled to a Nu Plasma Multi Collector ICP-MS using methods described in detail in appendix 1 of González-Jiménez et al. (2013b).

1.4 Zircon preparation and analysis

One hand specimen (ca 1 kg) of massive chromitite from Luobusa ore body no. 2 was disaggregated along grain boundaries by electrostatic comminution (selFrag apparatus); 28 euhedral zircons (≤150 μm in length) were retrieved from the comminuted material by magnetic separation and hand-picking. BSE and CL images were obtained (fig. 5.1.1).

U-Pb data were collected by LAM-ICP-MS, and Hf-isotope data by LAM-MC-ICP-MS, following methods detailed by Belousova et al. (2010).

O isotope data were analysed by Cameca ion micropobe at the China Academy of Sciences, Beijing, following techniques described by Li et al. (2010) and Gao et al. (2014).

1.5 $Fe^{3+}/\Sigma Fe$ Mössbauer spectroscopy preparation and analysis

$Fe^{3+}/\Sigma Fe$ data were collected by Mössbauer spectroscopy at Bayerisches Geoinstitut, Germany.

One nodular and two massive chromitite samples with minimum serpentinisation were selected for Mössbauer analysis. A number of grains were selected from each sample to investigate sample homogeneity, including after treatment in HCl. The resulting grains were handpicked under a microscope and mounted on Mylar film with clear nail varnish in clusters of roughly 500 μm diameter and 100-200 μm thickness. Mössbauer spectra were recorded at room temperature (293 K) in transmission mode on a constant acceleration spectrometer with a nominal 370 MBq ^{57}Co high specific activity ("point") source in a 12-μm Rh matrix. Spectra were collected over 1-3 days. $Fe^{3+}/\Sigma Fe$ values were determined from the relative areas of components fitted to the Mössbauer spectra.

Twelve Mössbauer spectra in total were collected for the three samples analysed.

Appendix DR 2 Analytical Results for Chromitite

2.1 Major-element EMP data for chromite

Table DR2.1.1. Major element EMP data for chromite from the Luobusa Peridotite, Tibet

	Wt%														
Sample	**SiO_2**	**TiO_2**	**Al_2O_3**	**Cr_2O_3**	**V_2O_3**	**FeO_t**	**MgO**	**CaO**	**Na_2O**	**NiO**	**ZnO**	**Total**	**Mg#**	**Cr#**	**#**
LUOB12-01	0.05	0.20	10.20	61.48	0.08	13.76	14.29	0.01	0.03	0.09	b.d.l.	100.27	0.68	0.78	11
LUOB12-05	0.06	0.13	10.65	60.57	0.09	13.72	14.60	0.01	0.01	0.12	b.d.l.	100.00	0.69	0.77	25
LUOB12-06	0.02	0.11	14.46	57.60	0.17	12.97	14.86	0.01	0.01	0.14	b.d.l.	100.39	0.69	0.71	27
LUOB12-07	0.02	0.12	10.23	61.08	0.09	14.17	14.22	b.d.l.	0.01	0.11	b.d.l.	100.10	0.68	0.78	31
LUOB12-08	0.05	0.06	41.56	26.89	0.14	13.57	16.79	0.02	0.01	0.16	0.24	99.47	0.71	0.30	7
LUOB12-09	0.01	0.23	10.55	62.12	0.08	12.22	15.49	0.01	b.d.l.	0.19	b.d.l.	100.95	0.73	0.78	9
LUOB12-11	0.03	0.17	12.87	58.05	0.10	16.18	12.90	0.01	0.01	0.08	b.d.l.	100.46	0.61	0.73	17
LUOB12-12	0.03	0.20	11.06	60.66	0.09	14.50	13.72	0.01	b.d.l.	0.09	b.d.l.	100.40	0.65	0.77	12
LUOB12-15	0.02	0.17	12.33	58.59	0.11	16.67	12.04	0.01	0.01	0.08	b.d.l.	100.11	0.58	0.75	20
LUOB12-16	0.02	0.15	11.88	60.25	0.10	14.50	13.94	0.01	0.01	0.10	b.d.l.	101.03	0.66	0.76	4
LUOB12-17	0.04	0.19	11.26	59.40	0.09	15.66	13.51	0.01	0.01	0.09	b.d.l.	100.30	0.64	0.75	6
LUOB12-18	0.03	0.18	9.77	61.55	0.08	14.90	13.64	b.d.l.	0.01	0.10	b.d.l.	100.31	0.65	0.79	16
LUOB12-19	0.02	0.24	10.78	61.36	0.08	12.67	15.30	0.01	0.01	0.19	b.d.l.	100.68	0.72	0.77	12
LUOB12-20	0.02	0.24	9.99	61.11	0.08	16.39	12.52	b.d.l.	b.d.l.	0.09	b.d.l.	100.49	0.60	0.79	13

125 Table DR2.1.2. Major-element EMP data for chromite from the Antalya Complex, Turkey
126

	Wt%														
Sample	**SiO_2**	**TiO_2**	**Al_2O_3**	**Cr_2O_3**	**V_2O_3**	**FeO_t**	**MgO**	**CaO**	**Na_2O**	**NiO**	**ZnO**	**Total**	**Mg#**	**Cr#**	**#**
1TKV12-1C	0.01	0.30	18.67	48.98	0.12	17.30	13.70	0.01	0.01	0.11	b.d.l.	99.26	0.64	0.61	10
1TKV12-1I	0.02	0.31	18.97	51.75	0.13	14.29	14.69	b.d.l.	b.d.l.	0.14	b.d.l.	100.39	0.67	0.63	9
2TKV12-2	0.01	0.25	15.44	52.65	0.10	19.96	11.37	0.05	b.d.l.	0.10	b.d.l.	100.00	0.54	0.67	8
3TKV12-1A	0.01	0.30	17.26	51.52	0.11	17.20	13.15	b.d.l.	b.d.l.	0.11	b.d.l.	99.72	0.61	0.64	9
3TKV12-1D	0.02	0.31	17.13	49.89	0.10	18.20	13.55	0.01	b.d.l.	0.12	b.d.l.	99.38	0.62	0.62	6
5TKV12-2C	0.02	0.21	12.44	56.21	0.11	18.17	11.88	0.01	b.d.l.	0.08	0.09	99.22	0.57	0.73	12
5TKV12-2D	0.01	0.11	15.26	54.90	0.10	17.64	11.68	0.01	0.01	0.05	0.10	99.87	0.56	0.70	11
5TKV12-3A	0.02	0.12	15.99	54.38	0.11	17.55	11.65	0.01	0.01	0.07	0.09	100.00	0.55	0.69	10
14TKV12-1B	0.01	0.23	15.42	54.59	0.09	14.78	14.72	b.d.l.	0.01	0.14	b.d.l.	100.03	0.69	0.68	6
14TKV12-1C	0.03	0.24	16.84	54.16	0.11	14.23	14.28	0.01	0.01	0.09	b.d.l.	100.05	0.66	0.67	6
14TKV12-2C	0.01	0.31	15.05	54.97	0.18	16.47	13.43	b.d.l.	b.d.l.	0.11	b.d.l.	100.57	0.63	0.69	8
15TKV12-1B	0.02	0.27	12.31	55.62	0.13	19.88	11.50	b.d.l.	b.d.l.	0.08	b.d.l.	99.81	0.55	0.72	13
15TKV12-2A	0.02	0.29	12.73	56.28	0.13	17.88	12.58	b.d.l.	0.01	0.10	b.d.l.	100.06	0.60	0.72	11
15TKV12-2C	0.01	0.29	15.34	49.95	0.20	21.55	11.71	0.01	0.01	0.07	0.08	99.23	0.56	0.63	5
17TKV12-3D	0.02	0.15	20.79	47.94	0.10	15.57	14.07	0.01	b.d.l.	0.11	b.d.l.	98.79	0.65	0.59	10
17TKV12-3G	0.02	0.30	18.34	51.70	0.10	16.61	12.81	b.d.l.	b.d.l.	0.10	b.d.l.	100.04	0.60	0.64	7
18TKV12-2B	0.01	0.13	19.01	50.26	0.12	17.31	13.07	b.d.l.	0.01	0.11	0.06	100.09	0.61	0.62	5
18TKV12-2C	0.01	0.21	20.63	49.92	0.10	14.61	14.13	b.d.l.	b.d.l.	0.10	b.d.l.	99.75	0.65	0.61	6

2.2 *In situ* trace-element LAM-ICP-MS data for chromite

Table DR2.2.1. *In situ* trace-element LAM-ICP-MS data for chromite from the Luobusa Peridotite, Tibet

	Concentration (ppm)								
Sample	**Ga69**	**Ti47**	**Ni60**	**Zn66**	**Co59**	**Mn55**	**V51**	**Sc45**	**#**
LUOB12-01	18.0	1030	696	343	228	1100	440	5.47	16
LUOB12-05	20.2	732	936	390	176	975	529	4.52	15
LUOB12-06	25.5	627	1000	465	179	987	1080	5.79	16
LUOB12-07	19.9	640	815	415	193	1030	520	4.83	17
LUOB12-09	19.7	1238	1540	318	175	914	501	5.03	10
LUOB12-11	19.8	947	518	424	250	1440	540	4.08	12
LUOB12-12	20.3	1045	806	430	227	1330	514	4.88	10
LUOB12-15	20.7	1040	631	593	233	1330	594	5.09	4
LUOB12-16	21.6	980	826	511	240	1320	602	6.35	6
LUOB12-17	19.9	1170	713	376	262	1480	489	3.77	12
LUOB12-18	17.9	1060	731	392	222	1250	488	6.60	10
LUOB12-19	19.6	1330	1420	309	170	965	476	4.28	6
LUOB12-20	18.3	1350	589	422	263	1460	448	6.83	10

132 Table DR2.2.2. *In situ* trace-element LAM-ICP-MS data for chromite from the Antalya Complex, Turkey
133

	Concentration (ppm)								
Sample	Ga69	Ti	Ni	Zn66	Co	Mn	V	Sc	#
1TKV12-1C	38.0	1860	816	596	275	1540	790	6.37	12
1TKV12-1I	40.4	1860	1000	497	207	1220	849	2.42	11
3TKV12-1A	29.6	1690	733	608	277	1550	650	5.91	12
3TKV12-1D	30.2	1800	776	573	271	1540	633	6.69	11
5TKV12-2C	24.3	1330	411	995	289	1980	718	5.77	10
5TKV12-2D	23.4	683	374	990	295	1660	647	3.87	10
5TKV12-3A	25.2	720	461	1000	317	1820	695	4.32	9
14TKV12-1B	31.3	1370	947	389	194	1150	591	6.22	9
14TKV12-1C	32.4	1520	813	410	199	1200	665	4.79	12
14TKV12-2C	30.0	1504	768	388	212	1300	651	4.91	8
15TKV12-1B	25.6	1680	665	489	259	1720	763	8.21	13
15TKV12-2A	24.8	1790	712	416	233	1640	731	7.05	14
15TKV12-2C	38.0	1860	816	596	275	1540	790	6.37	15
17TKV12-3D	37.8	869	930	497	194	1250	630	5.20	12
17TKV12-3F	37.1	861	978	526	207	1340	723	2.59	12
17TKV12-3G	35.4	1890	771	489	240	1430	592	3.72	12
18TKV12-2A	33.9	578	771	680	209	1320	655	2.17	11
18TKV12-2B	34.3	675	611	720	212	1400	659	3.32	5
18TKV12-2C	35.3	1230	749	519	234	1330	657	3.53	11

2.3 $Fe^{3+}/\Sigma Fe$ Mössbauer spectroscopy for chromite

Table DR2.3.1. $Fe^{3+}/\Sigma Fe$ values obtained by Mössbauer spectroscopy for chromite from the Luobusa peridotite, Tibet

	Measured proportions		
Sample (microstructure)	**Average $Fe^{3+}/\Sigma Fe$**	**ESD***	**Range**
LUOB12-05 (nodular)	24	2	23-27
LUOB12-09 (massive)	33	5	33-47
LUOB12-19 (massive)	32	5	32-44

*Estimated Standard Deviation

Appendix DR3 Ca and Si inclusions

3.1 Light microscope images for Ca and Si inclusions in chromite

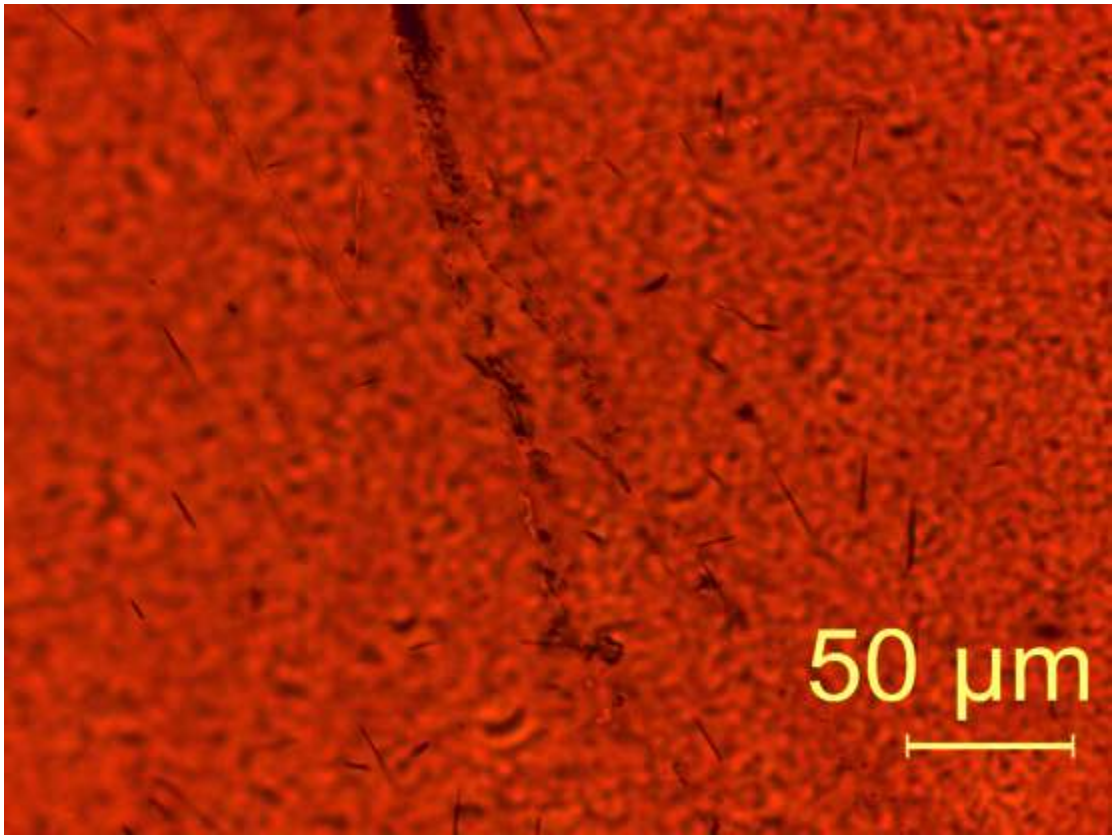

Figure DR3.1.1. Needle-shaped inclusions of diopside, enstatite and coesite in a massive chromite sample from the Luobusa peridotite, Tibet.

3.2 Major element EMP data for Ca and Si inclusions in chromite

Table DR3.2.1. Major-element SEM and EMP data for needle-shaped clinopyroxene in chromite from a massive chromitite sample from the Luobusa peridotite, Tibet

	Wt.%								
Size	SiO_2	TiO_2	Al_2O_3	Cr_2O_3	FeO	MgO	CaO	Na_2O	Total
50 µm	53.65	0.06	0.55	3.56	1.03	18.97	23.78	0.21	101.8
10 µm*	53.53		1.63	1.48	0.9	17.55	24.33	0.57	100
10 µm*	53.21		0.82	2.28	1.40	17.56	24.22	0.31	100

*SEM analyses; other is by EMP

Cr contents are maximum values, due to excitation of Cr by Fe X-rays

Appendix DR4 Analytical Results for laurites (Os-Ir-Ru sulphides)

4.1 BSE image data for laurites

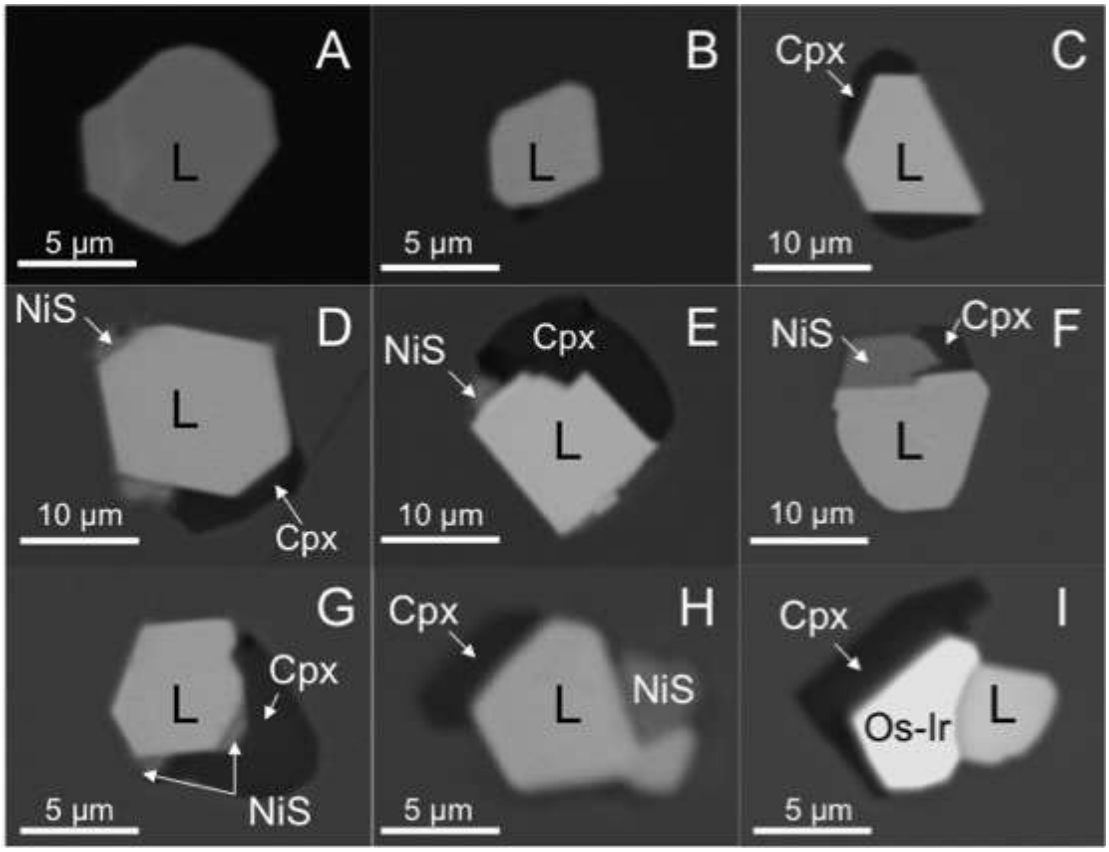

Figure DR4.1.1. Composite grains of Laurite, diopside and NiS in massive chromitite from ore body 11, in the eastern side of the Luobusa peridotite, Tibet.

4.2 Major-element EMP data for laurites

Table DR4.2.1. Major-element EMP data for Os-Ir-Ru sulphides in chromitite from the Luobusa Peridotite, Tibet

	Wt.%													
Sample (mineral)	**Os**	**Ir**	**Ru**	**Pt**	**Pd**	**Rh**	**Fe**	**Cr**	**Ni**	**Cu**	**Co**	**S**	**As**	**Total**
LA-623B-3-PTO2-1 (L[1])	24.3	12.9	27.6	0	0.98	0.29	0.66	2.29	0.64	0.09	0.03	31.5	0	101
LA-623B-3-PTO2-2 (L)	24.4	14.2	26.3	0	0.91	0.3	0.53	1.33	0.64	0.08	0.03	31.6	0	100
LA-623B-1-PTO1-2 (E[1])	56.9	10.1	4.4	0	0.17	0.24	0.83	3.09	0.28	0.17	0	25.9	0	102
LA-623B-1-PTO1-3 (L)	57.9	10.1	4.47	0	0.18	0.23	0.89	3.46	0.27	0.08	0	26.3	0	104
	At%													
	Os	**Ir**	**Ru**	**Pt**	**Pd**	**Rh**	**Fe**	**Cr**	**Ni**	**Cu**	**Co**	**S**	**As**	
LA-623B-3-PTO2-1 (L)	8.6	4.52	18.4	0	0.62	0.19	0.80	-	0.73	0.10	0.03	66.1	0	
LA-623B-3-PTO2-2 (L)	8.6	4.99	17.6	0	0.58	0.20	0.64	-	0.74	0.08	0.03	66.5	0	
LA-623B-1-PTO1-2 (E)	24.34	4.28	3.55	0	0.13	0.19	1.21	-	0.39	0.22	0.00	65.7	0	
LA-623B-1-PTO1-3 (L)	24.4	4.20	3.55	0	0.14	0.18	1.28	-	0.37	0.10	0.00	65.8	0	
	apfu													
	Os	**Ir**	**Ru**	**Pt**	**Rh**	**Fe**	**Ni**	**Σ**	**S**	**As**	**Ru#[2]**			
LA-623B-3-PTO2-1 (L)	0.26	0.14	0.55	0	0.01	0.02	0.02	1.00	2.00	0	0.68			
LA-623B-3-PTO2-2 (L)	0.26	0.15	0.53	0	0.01	0.02	0.02	0.99	2.01	0	0.67			
LA-623B-1-PTO1-2 (E)	0.73	0.13	0.11	0	0.01	0.04	0.01	1.02	1.98	0	0.13			
LA-623B-1-PTO1-3 (L)	0.73	0.13	0.11	0	0.01	0.04	0.01	1.02	1.98	0	0.13			

[1]L = laurite; E = erlichmanite; [2]Ru# = Ru/(Ru+Os)

4.3 *In situ* Re-Os isotope data for laurites

Table DR4.3.1. *In situ* Re-Os isotope data for Os-Ir-Ru sulphides in chromitite from the Luobusa chromitite, Tibet

	Measured ratios				Age data			
Sample	$^{187}Os/^{188}Os$	2σ	$^{187}Re/^{188}Os$	2σ	T_{Ma}^{ECR}(Ga)	2σ (Ga)	T_{RD}^{ECR}(Ga)	2σ (Ga)
LA-623B-1-PTO2	0.12436	0.00014	0.00004	0.00009	0.531	0.0029	0.531	0.0201
LA-623B-1-PTO3	0.11449	0.00019	0.00013	0.00013	1.91	0.0201	1.91	0.0260
LA-623B-2-PTO1	0.12583	0.00058	0.00001	0.00052	0.322	0.0261	0.322	0.0823
LA-623B-2-PTO2	0.12509	0.00090	0.00002	0.00020	0.428	0.0823	0.428	0.127
LA-623B-2-PTO3A	0.12588	0.00032	-0.00000	0.00016	0.3156	0.127	0.316	0.0454
LA-623B-2-PTO3	0.12611	0.00024	0.00004	0.00012	0.283	0.0454	0.283	0.0341
LA-586A-1-PTO1A	0.12421	0.00034	0.00084	0.00024	0.554	0.0341	0.553	0.0480
LA-586B-1-PTO1	0.12567	0.00030	0.00003	0.00005	0.345	0.0480	0.345	0.0425
LA-586B-1-PTO2	0.12609	0.00078	0.00033	0.00062	0.286	0.0426	0.286	0.111
LA-623B-PTO1	0.12561	0.00100	0.00125	0.00092	0.355	0.111	0.354	0.142
LA-623B-3-PTO2A	0.12382	0.00054	0.00028	0.00050	0.607	0.142	0.607	0.0762
LA-623B-3-PTO2B	0.12368	0.00012	0.00003	0.00005	0.626	0.0762	0.626	0.0166
LA-623B-3-PTO4	0.12515	0.00060	0.00014	0.00017	0.419	0.0800	0.419	0.0849

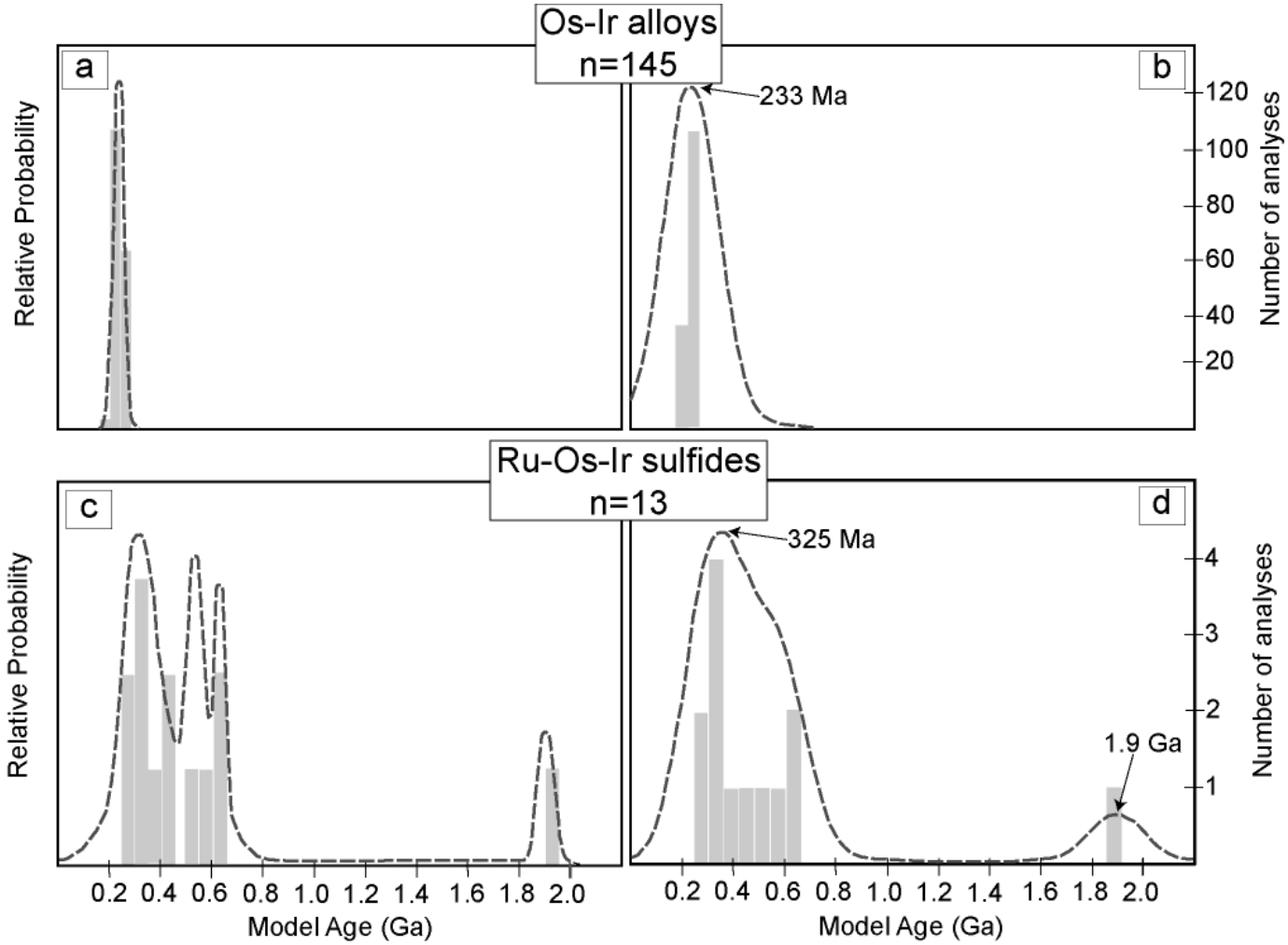

Figure DR4.3.1. Model age ranges for b) Os-Ir alloys (Shi et al., 2007), and d) laurite. (a) and (c) show the data with the analysed analytical errors (Table DR4.3.1); in (b) and (d) the uncertainties have been expanded to a uniform 0.1 Ga.

Appendix DR5 Analytical Results for Zircons

5.1 BSE and CL zircon image data for zircons

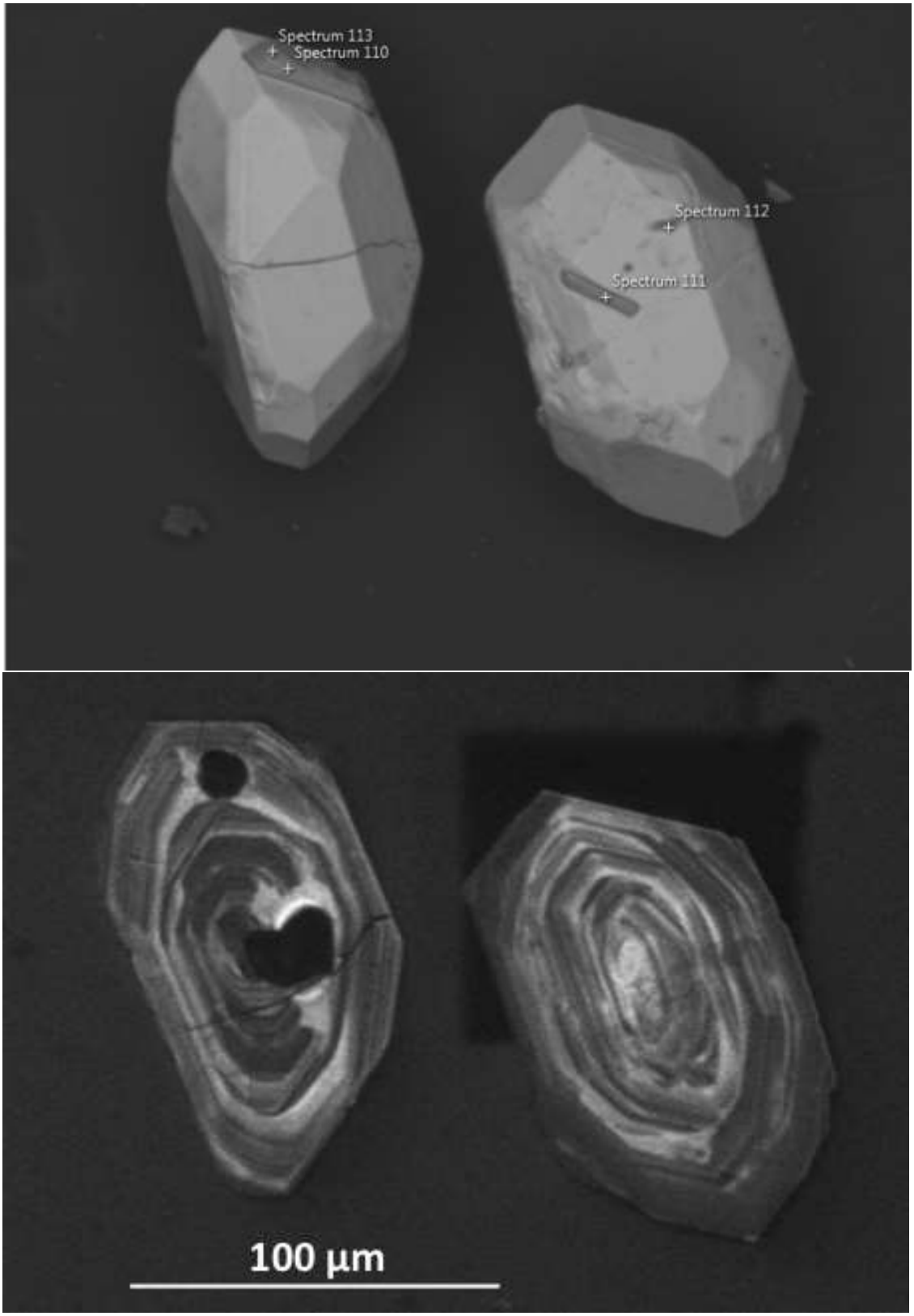

Figure DR5.1.1. Zircons from a Luobusa chromitite: (a) BSE image; (b) CL image. Dark inclusions are F-apatite; prisms of apatite are visible on both grains in (a).

5.2 *In situ* trace-element LAM-ICP-MS data for zircons

Table DR5.2.1. Trace-element data for zircons in chromitite from the Luobusa peridotite, Tibet

	Concentration (ppm)									
Element	**3A-02C**	**3A-02R**	**3A-07R**	**3A-08**	**3A-09**	**3A-10**	**3A-12**	**3A-14**	**3A-16**	**3A-19**
Y	1920	1200	1290	1440	3160	1200	1440	1490	4830	1690
Nb	4.98	4.58	6.39	3.02	7.15	2.73	5.33	6.67	9.90	9.91
La	3.69	2.62	8.59	7.31	1.00	2.37	0.00660	21.4	11.5	2.03
Ce	38.9	26.0	51.8	64.8	19.5	24.6	17.3	90.8	91.0	31.9
Pr	5.53	3.75	8.83	9.93	1.68	2.97	0.0670	16.0	9.92	1.99
Nd	41.0	28.2	71.0	82.8	17.7	24.0	1.65	99.8	70.4	15.5
Sm	24.5	15.4	35.1	30.9	18.1	13.3	2.99	29.7	40.8	8.50
Eu	2.45	1.65	3.02	3.21	2.26	2.08	0.84	2.54	8.41	0.94
Gd	45.9	26.8	47.5	46.2	66.7	29.1	19.6	42.1	125	26.0
Tb	12.2	7.33	9.40	<DL?	25.3	7.77	7.66	10.2	37.4	9.30
Dy	158	93.5	106	110	296	94.9	109	125	463	129
Ho	60.5	36.5	40.5	42.6	108	37.3	44.2	48.8	164	52.8
Er	290	176	192	204	480	179	224	231	723	261
Tm	65.9	41.5	42.9	45.2	105	41.9	53.5	51.7	152	60.6
Yb	666	417	417	459	1050	442	552	497	1390	603
Lu	121	79.5	78.9	98.6	158	83.8	105	94.2	234	116
Hf	8590	9290	9550	9530	9370	9200	8400	9730	8040	9420
Ta	1.48	1.57	2.22	1.07	2.28	1.08	1.78	2.47	2.72	3.30
Pb	43.9	56.2	29.6	24.1	37.8	26.6	28.2	28.2	65.1	43.8
Th	239	139	232	176	247	202	217	143	755	307

	Concentration (ppm)									
Element	**3A-02C**	**3A-02R**	**3A-07R**	**3A-08**	**3A-09**	**3A-10**	**3A-12**	**3A-14**	**3A-16**	**3A-19**
U	859	633	442	475	672	416	432	364	988	647
Th/U	0.280	0.220	0.530	0.370	0.370	0.480	0.500	0.390	0.760	0.470
U/Yb	1.29	1.52	1.06	1.04	0.640	0.940	0.780	0.730	0.710	1.07

Ti-in-zircon thermometer

The Ti-in-zircon thermometer of Watson and Harrison (2005) gives temperatures of 670–797 °C (Ti = 4–18 ppm).

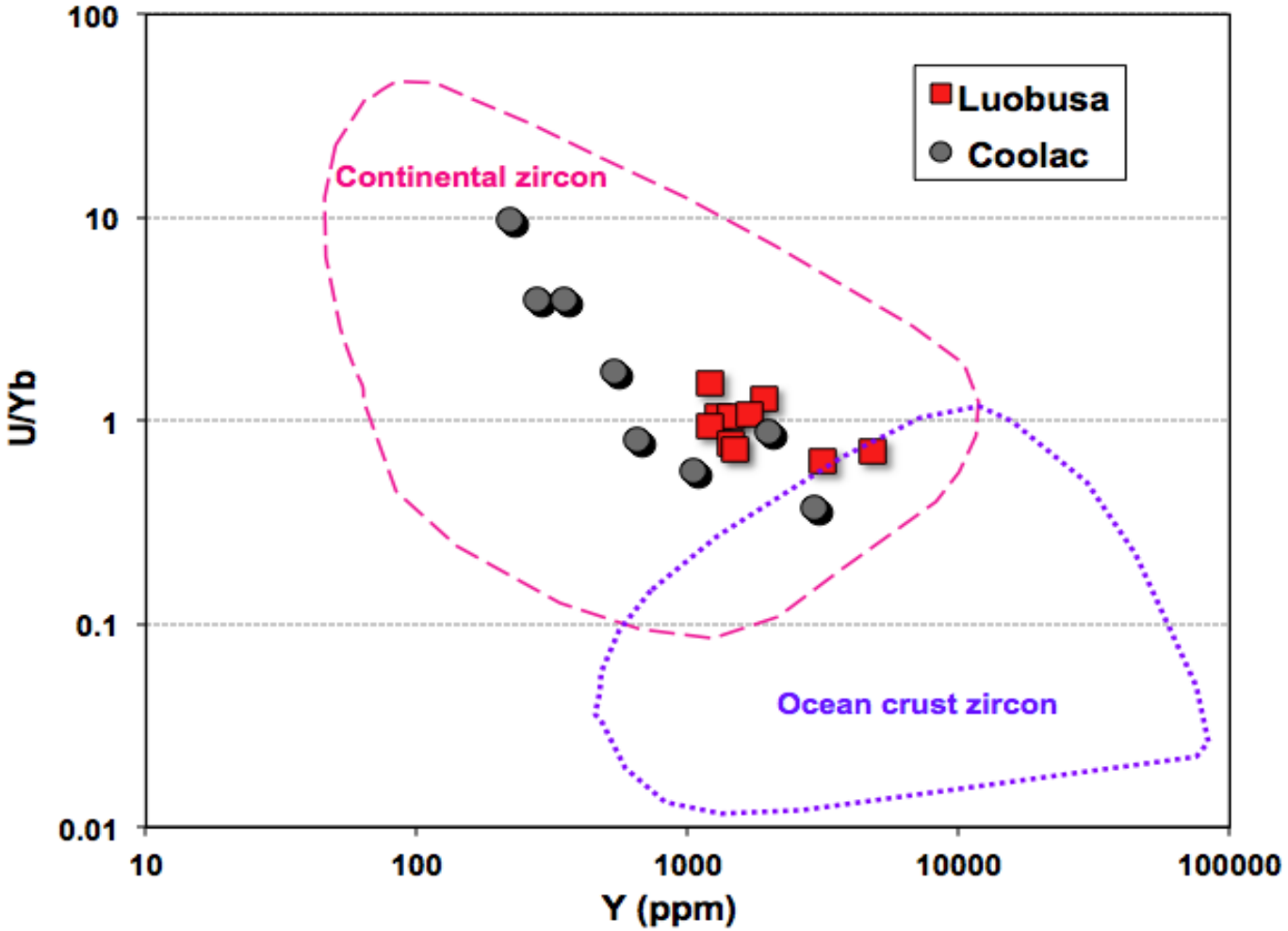

Figure DR5.2.1. U/Yb vs U values for zircon in chromitite from Luobusa (compared to zircons from chromitite from the Coolac ophiolite, Australia; Belousova et al., 2014) plot outside of the ocean-crust zircon field defined by Grimes et al. (2007), indicating crystallization from melts derived from continental crust (or subducted crustal material).

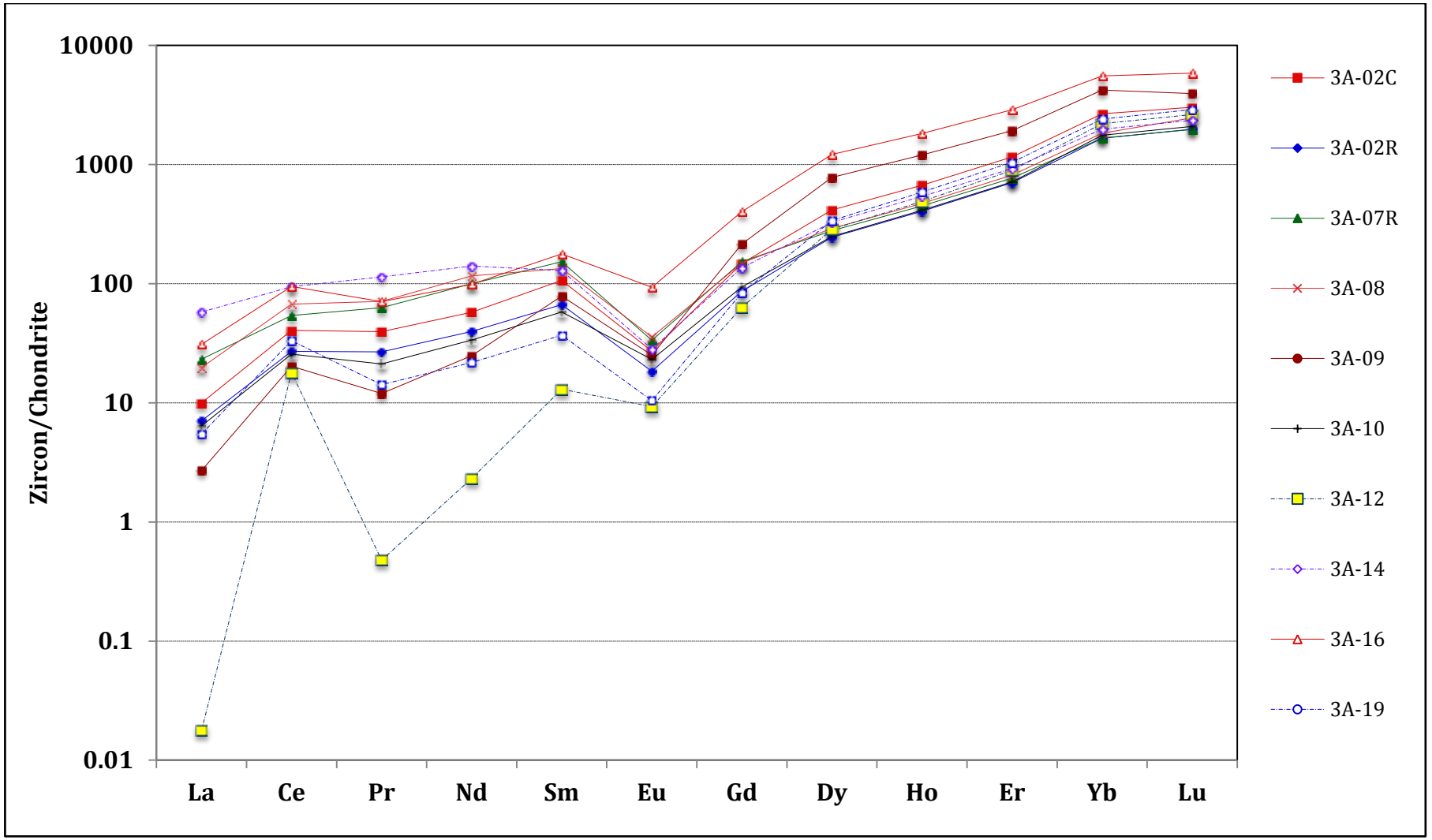

Figure DR5.2.2. Chondrite-normalised REE distributions in euhedral zircons in chromitite from Luobusa, Tibet.

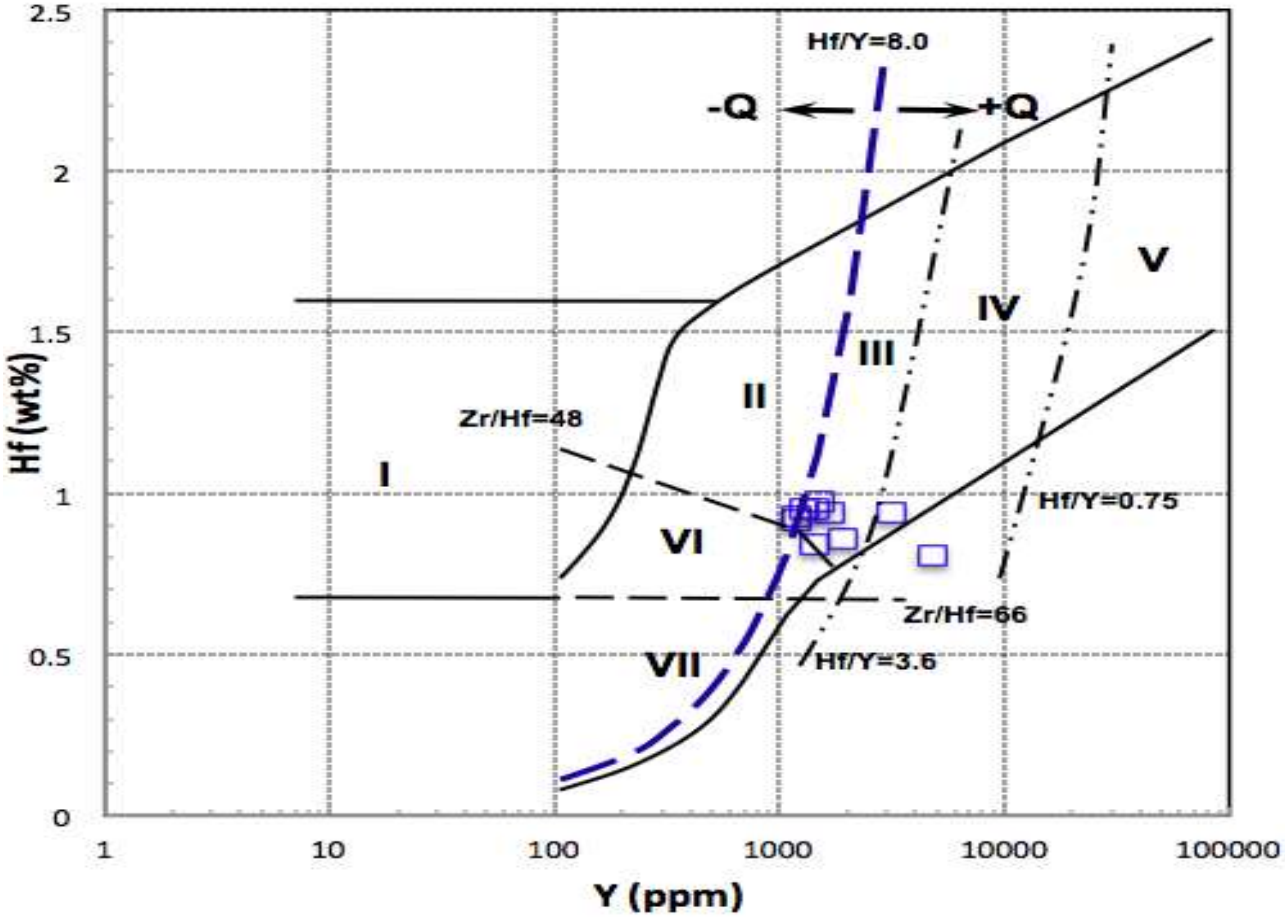

Figure DR5.2.3. Hf vs Y plot showing that zircon from Luobusa chromitite, Tibet is probably derived from plagioclase-bearing low-SiO_2 int.-mafic rock types (fields: I - kimberlites; II - ultrabasic, basic and intermediate rocks; III -quartz-bearing intermediate and felsic rocks; IV - felsic rocks with 'high' SiO2 content; V - greisens; VI - alkaline rocks and alkaline metasomatites of alkaline complexes; VII – carbonatites; Shnukov, et al., 1997).

5.3 U-Pb age LAM-ICP-MS data for zircons

Table DR5.3.1. Pb age LAM-ICP-MS data for zircons in chromitite from the Luobusa peridotite, Tibet

	Corrected Ratios					Corrected Ages (Ma)							
Sample	$Pb^{207/206}$	Pb^{207}/U^{235}	Pb^{206}/U^{238}	Pb^{208}/Th^{232}	U^{238}/Th^{232}	$Pb^{207/206}$	1s	Pb^{207}/U^{235}	1s	Pb^{206}/U^{238}	1s	Pb^{208}/Th^{232}	1s
3A-02C*	0.114	0.63	0.040	0.050	3.5	1864	58	493	12	252	4	994	50
3A-02R*	0.106	0.46	0.032	0.034	3.8	1727	70	384	11	200	4	672	40
3A-07R	0.055	0.44	0.059	0.016	1.8	408	53	373	7	368	5	327	11
3A-08	0.054	0.42	0.057	0.015	1.8	385	134	360	17	356	8	298	26
3A-09*	0.074	0.60	0.059	0.019	2.5	1036	199	475	34	367	12	387	54
3A-10	0.054	0.45	0.061	0.019	1.9	355	84	378	11	382	6	384	21
3A-12	0.056	0.46	0.060	0.019	2.0	437	67	387	9	379	5	381	17
3A-14	0.059	0.48	0.059	0.018	2.2	582	88	400	13	369	6	354	22
3A-16	0.055	0.48	0.063	0.018	1.2	430	110	397	15	391	7	363	30
3A-19	0.053	0.45	0.061	0.020	2.0	320	59	375	8	384	5	398	17

*rejected analyses

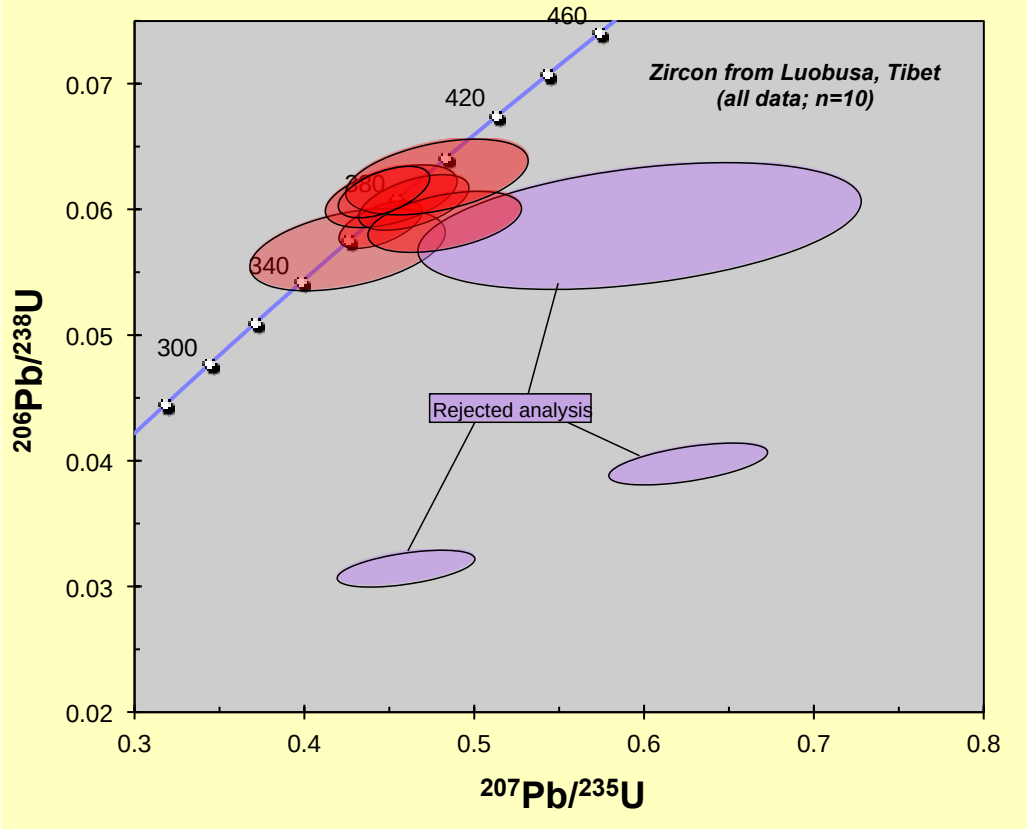

Figure DR5.3.1. Concordia plot for zircon from Luobusa ophiolite, Tibet (n=10; including rejected analyses).

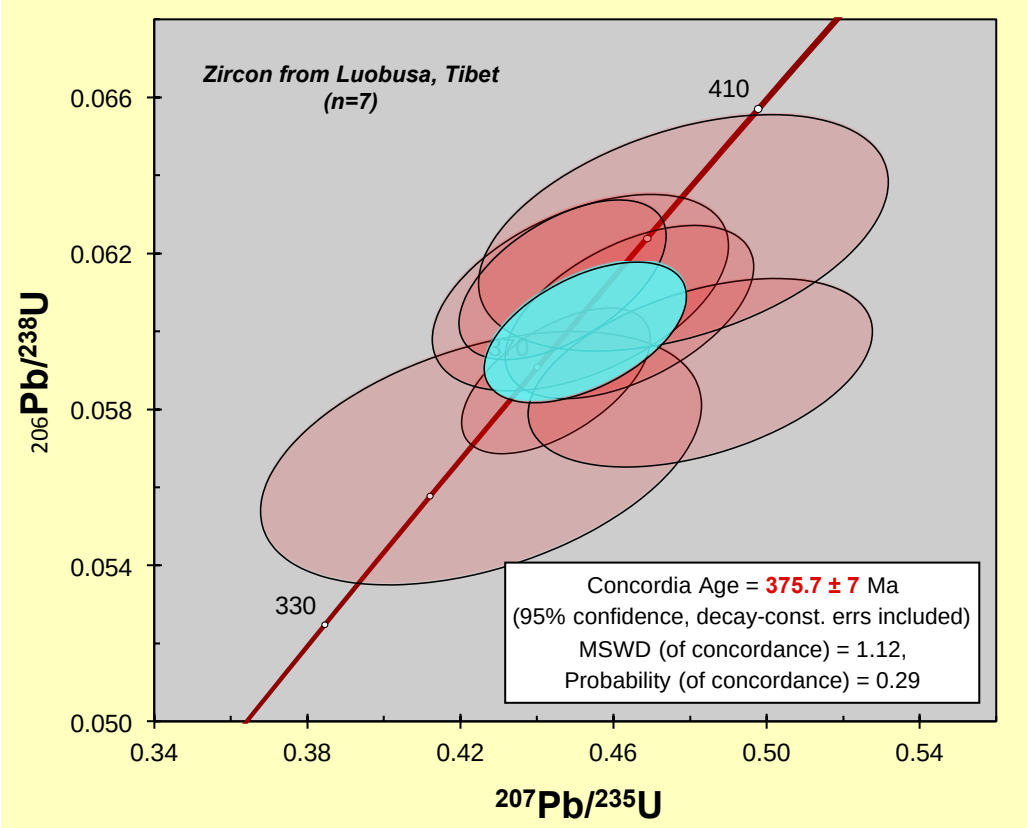

Figure DR5.3.2. Concordia plot for zircon from Luobusa ophiolite, Tibet (n=7; excluding rejected analyses (see **A5.3**).

5.4 Hf- and O-isotope LAM-ICP-MS and LAM-MC-ICP-MS data for zircons

Table DR5.4.1. Hf-isotope LAM-ICP-MS data for zircons in chromitite from Luobusa chromitite, Tibet

	Hf-isotope LAM-ICP-MS data									O-isotope LAM-MC-ICP-MS data		
	Measured ratios				Age data							
Sample	$^{176}Hf/^{177}Hf$	1SE	$^{176}Lu/^{177}Hf$	$^{176}Yb/^{177}Hf$	$Hf_{initial}$	εHf(T)	1SE	T_{DM}(Ga)	T_{DMC}^{*}(Ga)	$\delta^{18}O$	2SE	
3A-02	0.282770	0.000078	0.001114	0.034966	0.282762	7.91	2.7	0.69	0.87	-	-	rim
3A-04	0.282784	0.000019	0.002038	0.059303	0.282770	8.18	0.67	0.68	0.86	5.62	0.39	core
	-	-	-	-	-	-	-	-	-	5.50	0.41	rim
	-	-	-	-	-	-	-	-	-	5.37	0.44	rim
3A-05	-	-	-	-	-	-	-	-	-	5.95	0.42	core
3A-06	0.282740	0.000030	0.001695	0.059280	0.282728	6.71	1.1	1.74	0.95	6.14	0.41	core
	-	-	-	-	-	-	-	-	-	6.38	0.49	core
3A-07	-	-	-	-	-	-	-	-	-	6.39	0.43	core
	0.282780	0.000021	0.001302	0.040504	0.282771	8.22	0.74	0.68	0.86	5.83	0.52	rim
3A-08	0.282782	0.000042	0.001611	0.058045	0.282771	8.22	1.5	0.68	0.86	5.94	0.56	core
3A-10	0.282950	0.000079	0.001010	0.026497	0.282943	14.31	2.8	0.43	0.46	-	-	
3A-12	0.282808	0.000029	0.001875	0.051747	0.282795	9.07	1.0	0.64	0.80	-	-	
3A-14	0.282821	0.000018	0.001295	0.039158	0.282812	9.67	0.62	0.62	0.76	4.83	0.58	core
3A-15	0.282725	0.000025	0.001684	0.058681	0.282713	6.18	0.88	0.76	0.99	6.29	0.48	core
	-	-	-	-	-	-	-	-	-	6.34	0.60	rim
3A-16	0.282896	0.000390	0.003002	0.106927	0.282875	11.9	14	0.53	0.62	6.35	0.33	rim
3A-18	0.282859	0.000040	0.002457	0.098413	0.282842	10.73	1.4	0.58	0.69	6.51	0.40	core

	Hf-isotope LAM-ICP-MS data									O-isotope LAM-MC-ICP-MS data		
	Measured ratios				Age data							
Sample	$^{176}Hf/^{177}Hf$	1SE	$^{176}Lu/^{177}Hf$	$^{176}Yb/^{177}Hf$	$Hf_{initial}$	εHf(T)	1SE	T_{DM}(Ga)	T_{DMC}^{*}(Ga)	$\delta^{18}O$	2SE	
	0.282668	0.000046	0.003275	0.104725	0.282645	3.77	1.6	0.88	1.14	8.19	0.29	rim
3A-19	0.282805	0.000017	0.001612	0.047060	0.282794	9.03	0.60	0.64	0.780	6.36	0.39	rim
	-	-	-	-	-	-	-	-	-	6.36	0.30	rim
3A-21	0.282638	0.000048	0.002475	0.093825	0.282621	2.9	1.7	0.91	1.20	8.06	0.32	core
	0.282809	0.000087	0.001219	0.038571	0.282800	9.27	3.1	0.63	0.79	7.00	0.34	rim
	0.282839	0.000037	0.002155	0.077979	0.282824	10.11	1.3	0.60	0.73	7.14	0.30	rim
3A-22	0.282778	0.000017	0.001969	0.065175	0.282764	7.98	0.60	0.69	0.87	7.38	0.25	rim

221 *Crustal model age with respect to the depleted mantle

222 Lu–Hf CHUR from Bouvier et al. (2008), using 176Lu/177Hf CHUR, today 0.0336±1 and 176Hf/177Hf CHUR today 0.282785±11; εHf

223 calculated from Scherer et al. (2001) using ^{176}Lu decay constant $1.865x10^{-11}$.

224

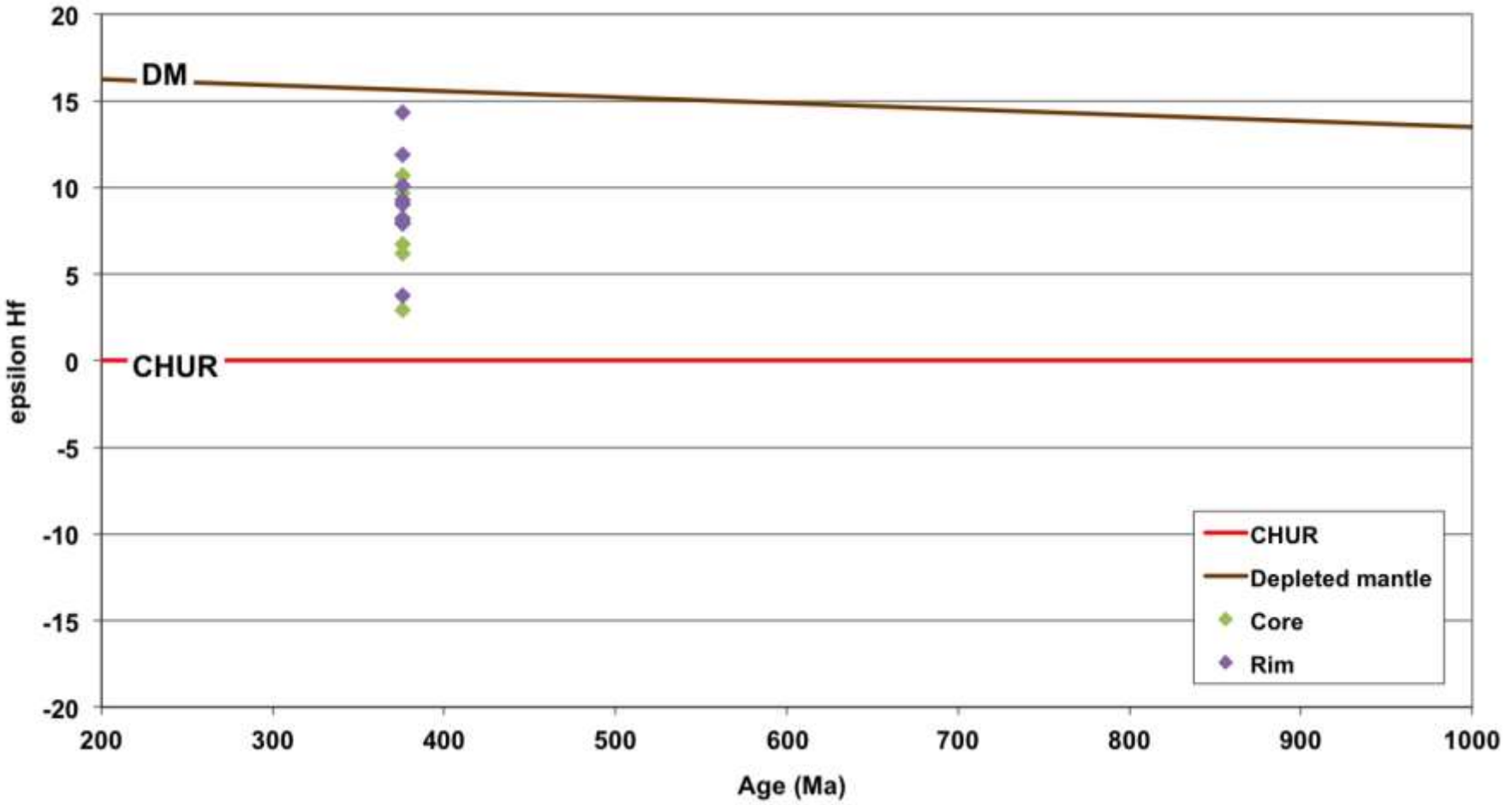

225

226 Figure DR5.4.1. εHf for zircons in chromitite from the Luobusa peridotite, Tibet.

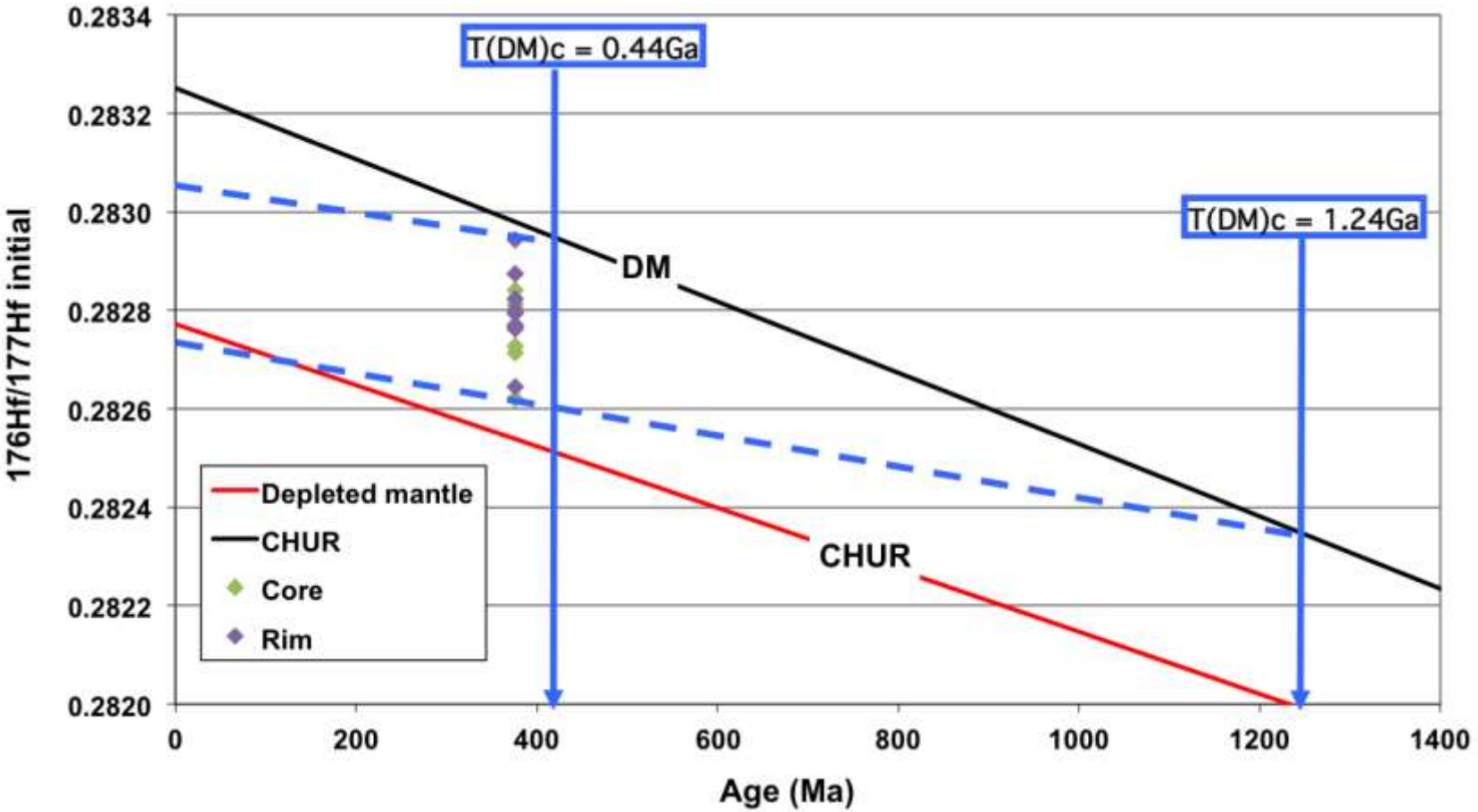

227
228 Figure DR5.4.2. Crustal Hf model ages for zircons in chromitite from the Luobusa peridotite, Tibet.

Appendix DR6 Thermo-mechanical Model

Fig. DR6 shows three snapshots from a simulation of the geodynamic behaviour of a simulated lithospheric domain, volumetrically dominated by highly depleted (buoyant) peridotites, in a collisional setting, where a large passive upwelling occurs in response to slab roll-back during subduction. The initial long-wavelength upwelling (Fig. 3a) is a consequence of the initial steepening of the slab concomitant with roll-back; these features have been observed in a large number of simulations with different viscosity parameters and boundary conditions (Afonso and Zlotnik, 2011; Moresi et al., 2014). Since the viscosity is non-Newtonian, the upwelling of hot and buoyant mantle material develops a self-maintained low-viscosity channel where velocities are relatively large (~6-8 cm yr^{-1}). This upwelling is a long-lived feature that can bring material from the TZ to the uppermost mantle in $\lesssim$10 Ma, provided the subduction system remains active for at least that long. Such large-scale passive upwelling is not observed in models without the initial steepening and roll-back of the slab. Therefore, this combination seems to be a prerequisite for the exhumation of deep mantle material in the fore-arc side of such subduction systems. In a 3D scenario, the lateral "escape" of asthenospheric mantle observed in Fig. 3c would probably occur parallel to the trench, which would facilitate the entrainment of deep mantle material along the suture zone.

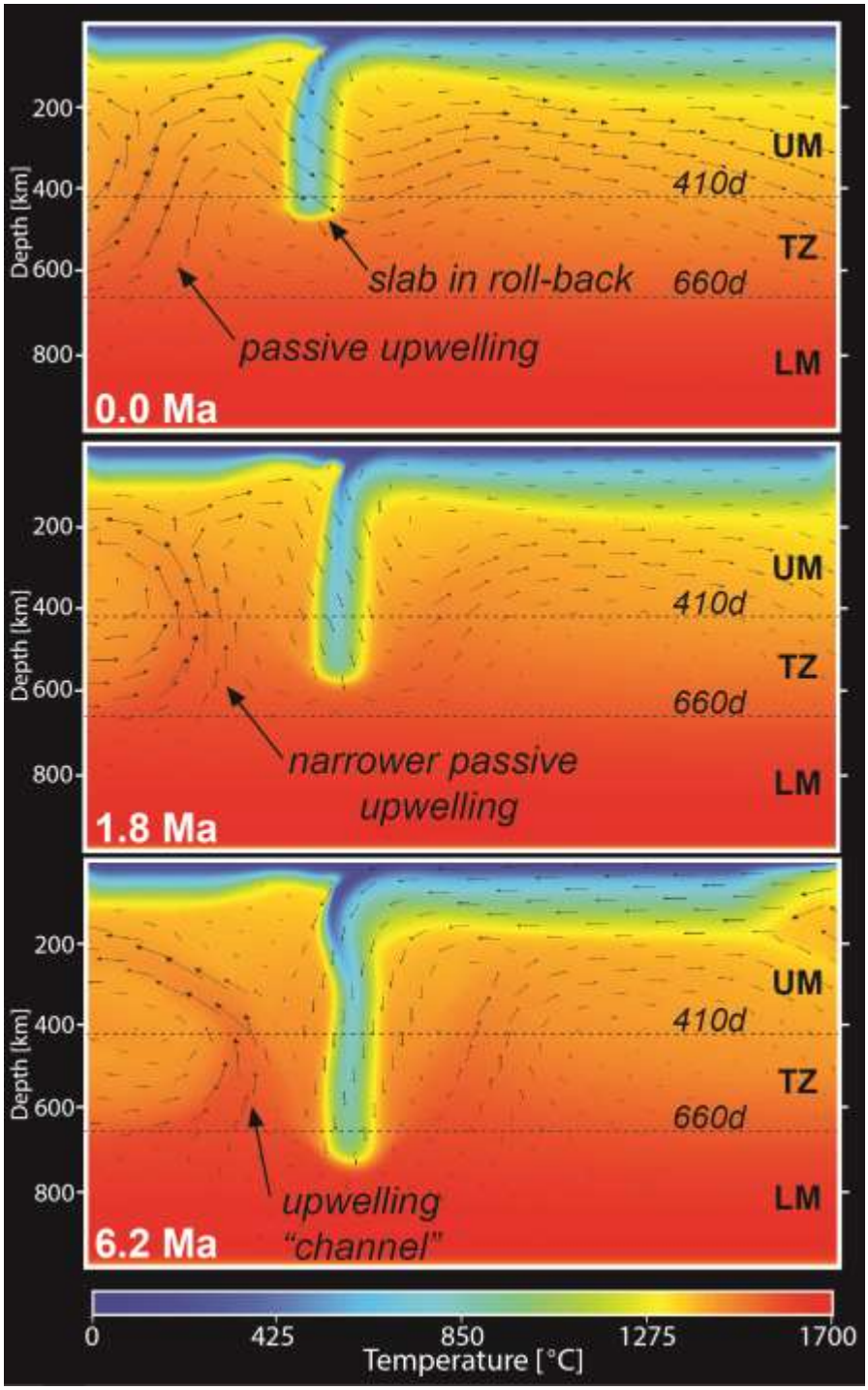

Figure DR6.1. 2D simulation of a collisional setting resulting in a relatively large passive upwelling in response to slab roll-back/subduction (see Afonso and Zlotnik (2011) for details on the thermodynamically consistent numerical implementation, model setup, rheological parameters, and boundary conditions). The simulation starts (a) with a 45^{o}-dipping slab in the upper mantle. Non-Newtonian viscosity results in upwelling of hot mantle material at ~6-8 cm yr^{-1}. 410d and 660d refer to Transition Zone depths.

REFERENCES CITED

Afonso, J. C., and Zlotnik, S., 2011, The subductability of the continental lithosphere: the before and after story; in Brown, D., and Ryan, P. D., Arc-continent collision, Frontiers in Earth Sciences, p. 53-86.

Belousova, E. A., Kostitsyn, Y. A., Griffin, W. L., Begg, G. C., O'Reilly, S. Y., Pearson, N. J., 2010, The growth of the continental crust: constraints from zircon Hf-isotope data, Lithos, v. 119, no. 3, p. 457-466.

Belousova, E. A., González-Jiménez, J. M., Graham, I., Griffin, W. L., O'Reilly, S. Y., Pearson, N. J., 2014, Crustal-mantle interaction in the Tumut region of the Lachlan fold belt, Southeastern Australia: A synthesis of new isotopic information (Re-Os, U-Pb, Lu-Hf and O), 12th International Platinum Symposium, Yekaterinburg, Urals, Russia

Bouvier, A., Vervoort, J. D., Patchett, P. J., 2008, The Lu–Hf and Sm–Nd isotopic composition of CHUR: Constraints from unequilibrated chondrites and implications for the bulk composition of terrestrial planets, *EPSL*, v. 273, p. 48-57.

González-Jiménez, J. M., Marchesi, C., Griffin, W. L., Gutiérrez-Narbona, R., Lorand, J-P., O'Reilly, S. Y., Garrido, C. J., Gervilla, F., Pearson, N. J., Hidas, K., 2013a, Transfer of Os isotopic signatures from peridotite to chromitite in the subcontinental mantle: Insights from in situ analysis of platinum-group and base-metal minerals (Ojén peridotite massif, southern Spain), Lithos, v. 164-167, p. 74-85.

González-Jiménez, J. M., Locmelis, M., Belousova, E., Griffin, W. L., Gervilla, F., Kerestedjian, T. N., O'Reilly, S. Y., Pearson, N. J., and Sergeeva. I., 2013b, Genesis and tectonic implications of podiform chromitites in the metamorphosed ultramafic massif of Dobromirtsi (Bulgaria), *Gondwana Research*, (in press), http://dx.doi.org/10.1016/j.gr.2013.09.020.

Grimes, C. B., John, B. E., Kelemen, P. B., Mazdab, F. K., Wooden, J. L., Cheadle, M. J., Hanghøj, K., Schwartz, J. J., 2007, Trace element chemistry of zircons from oceanic crust: A method for distinguishing detrital zircon provenance, *Geology*, v. 35, no. 7, p. 643-646.

Moresi, L., Betts, P. G., Miller, M. S., and Cayley, R. A. 2014, Dynamics of continental accretion, Nature, v. 508, no. 7495, p. 245-248.

Norman M. D., Pearson N. J., Sharma A., and Griffin W. L., 1996, Quantitative analysis of trace elements in geological materials by laser ablation ICPMS: Instrumental operating conditions and calibration values of NIST glasses, Geostand. News, v. 20, p. 247–261.

Norman M. D., Griffin W. L., Pearson N. J., Garcia M. O., and O'Reilly S. Y., 1998, Quantitative analysis of trace element abundances in glasses and minerals: A comparison of laser ablation ICPMS, solution ICPMS, proton microprobe, and electron micro-probe data, Journal of Analytical Atomic Spectroscopy, v. 13, p. 477–482.

Scherer, E., Münker, C., & Mezger, K., 2001, Calibration of the lutetium-hafnium clock, *Science*, v. 293, no. 5530, p. 683-687.

Shnukov, S. E., Andreev, A. V., Savenok, S. P., 1997, Admixture elements in zircons and apatites: a tool for provenance studies of terrigenous sedimentary rocks, European Union of Geosciences (EUG 9), 23-24 March 1997, Strasbourg, Abstract 65/4P16:597.

Watson, E.B., and Harrison, T.M., 2005, Zircon Thermometer Reveals Minimum Melting Conditions on Earliest Earth: Science, v. 308, no. 5723, p. 841–844, doi:10.1126/science.1110873.